PERGAMON

International Journal of Heat and Mass Transfer 45 (2002) 667–678

International Journal of HEAT and MASS TRANSFER

www.elsevier.com/locate/ijhmt

Active control of natural convection in a fluid layer with volume heat dissipation

T. Marimbordes, A. Ould El Moctar, H. Peerhossaini *

Thermofluids and complex flows research group, Laboratoire de Thermocinétique, CNRS-UMR 6607, Ecole polytechnique de l'université de Nantes, B.P. 50609, Rue Christian Pauc, F-44306 Nantes Cedex 3, France

Received 20 December 1999; received in revised form 23 February 2001

Abstract

A fluid layer subjected to an internal heating source and cooled from above and below is studied. Using linear stability analysis and numerical simulation it is shown that the critical Rayleigh number related to the bifurcation from the motionless conductive state to a convective state can be increased by controlling the heating power. A feedback-control strategy using the deviation of the real fluid temperature from that of the associated conductive state is applied for this purpose.

1. Introduction

Active control of fluid dynamics and heat transfer phenomena has a strategic position in current research. The aim, in most of these activities, is to control the drag on bodies, to increase or decrease mixing, or to control heat transfer between a domain and its environment.

In general, active flow control can be seen as imposing a pseudo-stable state (as opposed to the naturally stable state) on a system by perturbing its energetic (mechanical or thermal) state in time and/or space. The perturbation is imposed by importing energy from the exterior, conditioned by information extracted from the fluid domain. The range of control variables influencing the flow or heat transfer is very large and so is the choice of control strategies.

One of the most common techniques of controlling fluid flows is by mass injection on the wall. Many numerical investigations are reported in the literature. Joslin et al. [1,2] studied wave growth control by suction and blowing in a fully developed channel flow in order to keep the drag force at a given value. Their feedback rule searches for an optimal control by minimizing a cost function depending on the value of the wall shear stress measured in one or two positions and also normal-to-wall velocity generated by actuators.

Another technique for active control of flow uses wall deformation or wall movement. Choi et al. [3] used this technique in order to reduce wall drag in a turbulent flow. They used the vibration normal to the flow of the upper wall of a channel to control the flow structure.

Heat transfer from a wall to the flow can also be used for flow control. The transition to turbulence in a boundary layer is among the various phenomena that can be controlled by heat transport from the wall. Computational studies by Kral et al. [4] showed the real efficacy of this technique. Active control of Rayleigh–Bènard thermoconvective instability is another example of this type. Numerical and theoretical work by Singer et al. [5] and Tang et al. [6] have shown that by dividing the lower boundary into strips and modulating the boundary temperature as a function of the temperature of sensors located in selected positions in the fluid layer, it is possible to retard the threshold of instability in the cavity. Experimental results of Howle [7] using a control strategy similar to that of Tang et al. showed an almost total elimination of convective motion. Howle's [7] configuration is close to that studied here, except that in the present work a source of volume heat dissipation is introduced into the fluid.

* Corresponding author. Tel.: +33-2-4068-3140; fax: +33-2-4068-3141.

E-mail address: hassan.peerhossaini@polytech.univ-nantes.fr (H. Peerhossaini).

0017-9310/02/$ - see front matter
PII: S0017-9310(01)00182-X

Nomenclature

a	wave number
a_x	wave number in $\vec{i}$ direction
a_y	wave number in $\vec{j}$ direction
C_p	thermal capacity (J kg^{-1} °C^{-1})
d	spacing between the two parallel plates (m)
E	electric field magnitude (V m^{-1})
$\vec{g}$	acceleration of gravity (m s^{-2})
G	dimensionless control coefficient
G_d	control coefficient (s^{-1})
$\vec{i}, \vec{j}, \vec{k}$	space directions
$\dot{q}$	specific heating power (°C s^{-1})
$\dot{q}_1$	constant part of controlled specific heating power (°C s^{-1})
$\dot{q}_2$	fluctuating part of controlled specific heating power (°C s^{-1})
s	temporal growth rate (s^{-1})
T_0	wall temperature (°C)
u, v, w	velocity components (m s^{-1})
$\vec{v}$	velocity vector
x, y, z	space coordinates (m)
z_i	z-position where the data are obtained (m)

Greek symbols

α	thermal expansion coefficient (°C^{-1})
θ	temperature (°C)
θ_{cond}	conductive temperature (°C)
$\theta_{cond_{z_i}}$	conductive temperature at $z = z_i$ (°C)
θ_{z_i}	real convective temperature at $z = z_i$ (°C)
$D\Theta$	conductive temperature gradient (°C m^{-1})
κ	thermal diffusivity (m^2 s^{-1})
ν	kinematic viscosity (m^2 s^{-1})
ρ	density (kg m^{-3})
$\bar{\rho}$	density at $\theta = 0$ (kg m^{-3})
σ	electric conductivity (Ω^{-1} m^{-1})
$\bar{\bar{\tau}}$	shear stress tensor

Nondimensional numbers

Ra	Rayleigh number
Pr	Prandtl number

This paper concerns the active control of thermoconvective instability in a fluid cavity subjected to uniformly distributed volume heating generated by direct resistance heating. Unlike the classical Rayleigh–Bènard stability of a cavity with differentially heated horizontal walls, the present configuration has received little attention in the past years.

A fluid layer separating two parallel horizontal plates is considered (Fig. 1(a)). The fluid is subject to volume heating. Heating can be generated by passing an electric current (electric field magnitude E) through a conducting fluid (electric conductivity σ) [8,9]: the electric energy dissipated in the fluid by the Joule effect (σE^2) is then transformed to heat. Unlike dielectric fluids, in conducting fluids the effect of the electric force is negligible compared to that of buoyancy. The temperature of the upper and the lower plates, considered the cold temperature, is kept constant, and the lateral walls are thermally insulated. The temperature profile in the fluid layer due to volume heat generation is parabolic with the maximum in the center. Thus, the lower half of the fluid layer is stable while the upper half is susceptible to thermoconvective instability if the heating power exceeds a critical value. This work concerns the active control of the stability in the upper half of the fluid layer and is aimed at controlling the instability threshold by keeping the conductive state above the critical heating power. The conductive state is characterized by a motionless fluid layer in which the temperature has a parabolic profile between the two parallel plates.

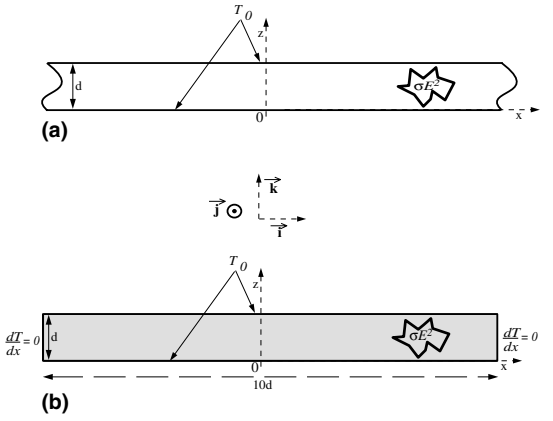

Fig. 1. (a) Fluid layer and sign convention for the theoretical study, (b) cavity and sign convention for the numerical approach.

The governing equation of the conductive state is the heat equation:

$$\Delta\theta = -\frac{\dot{q}}{\kappa}. \tag{1}$$

Here $\dot{q} = \sigma E^2/\rho C_p$ is the specific heating power, where σE^2 is the global heating power (W m^{-3}) applied to the system and θ is the difference between the fluid temperature and the wall temperature T_0. The symmetry of the lateral boundary conditions implies a one-dimensional heat conduction phenomenon across the fluid layer with the analytic solution for temperature

$$\theta = \frac{\dot{q}}{2\kappa} z(d-z). \tag{2}$$

From now on this state, the *conductive state*, is used as the reference temperature.

Beyond a critical heating power, the upper half of the fluid layer becomes unstable and a cellular motion due to convection begins. The temperature distribution across the fluid layer then deviates from the parabolic distribution. The aim here is to find heating power conditions that eliminate the convective motion so that the parabolic temperature distribution is reestablished across the fluid layer.

This paper is organized as follows. In Section 2 a linear stability analysis is carried out to establish the stability limits of the conductive state. This analysis is similar to that carried out by Roberts [10] and Debler [11] on a cavity subjected to internal heating but with upper and lower walls at different temperatures. In Section 3, after choosing a control strategy, the linear stability of the controlled system is developed for an unbounded layer (Fig. 1(a)). Numerical calculations are reported in Section 4. Our algorithm is first tested by verifying the instability threshold for the uncontrolled system. The efficacy of the control strategy is then examined by numerical simulation of active control of convection in a two-dimensional cavity (Fig. 1(b)).

2. Linear stability analysis: uncontrolled cavity

2.1. Problem formulation

The analysis starts with the equation of energy in its general form

$$\frac{\mathrm{d}\theta}{\mathrm{d}t} = \vec{\nabla}\cdot(\kappa\vec{\nabla}\theta) + \dot{q} \tag{3}$$

with $\mathrm{d}\theta/\mathrm{d}t$ the total derivative of θ. It is assumed that the thermophysical properties of the fluid are constant in the range of temperatures studied, except for the density in the volume force term

$$\rho = \bar{\rho}(1-\alpha\theta). \tag{4}$$

The momentum and continuity equations with the Boussinesq approximation can be written as

$$\frac{\mathrm{d}\vec{v}}{\mathrm{d}t} = -\vec{\nabla}\left(\frac{p}{\bar{\rho}} + gz\right) - \alpha g\theta\vec{k} + \frac{\vec{\nabla}\cdot\bar{\bar{\tau}}}{\bar{\rho}}, \tag{5}$$

$$\vec{\nabla}\cdot(\rho\vec{v}) = 0. \tag{6}$$

The temperature and velocity boundary conditions are:

$$\begin{array}{ll} \theta = 0 & \text{at } z = 0, d, \\ \vec{v} = \frac{\partial\vec{v}}{\partial z} = \vec{0} & \text{at } z = 0, d. \end{array} \tag{7}$$

2.2. Stability limits of the uncontrolled system

The velocity, temperature and pressure in the system of Eqs. (3), (5), and (6) are perturbed by infinitesimal disturbances:

$$\theta(t,x,y,z) = \Theta(x,y,z) + \theta'(t,x,y,z),$$

$$\vec{v}(t,x,y,z) = \vec{V}(x,y,z) + \vec{v}'(t,x,y,z),$$

$$p(t,x,y,z) = P(x,y,z) + p'(t,x,y,z).$$

The $\mathcal{O}(1)$ equations for disturbances are obtained by subtracting the equations of the nonperturbed state and are then linearized. The variables are nondimensionalized by using the specific heating power, the thermal diffusivity and the characteristic length of the cavity:

$$w^* = \frac{wd}{\kappa}, \quad \theta^* = \frac{\theta\kappa}{\dot{q}d^2}, \quad t^* = \frac{t\kappa}{d^2}, \quad z^* = \frac{z}{d}, \quad p^* = \frac{pd^2}{\bar{\rho}\kappa^2}.$$

The dimensionless system of equations then follows:

$$\frac{\partial\theta'^*}{\partial t^*} + w'^*\frac{\partial\Theta^*}{\partial z^*} = \Delta^*\theta'^*, \tag{8}$$

$$\frac{\mathrm{d}\vec{v}'^*}{\mathrm{d}t^*} = -\vec{\nabla}^* p'^* - Ra\,Pr\,\theta'^*\vec{k} + Pr\,\Delta^*\vec{v}'^*, \tag{9}$$

where Ra and Pr are the Rayleigh and Prandtl numbers defined as

$$Ra = \frac{\alpha g\dot{q}d^5}{\kappa^2 v}, \quad Pr = \frac{v}{\kappa}.$$

For the sake of convenience $(')$ and $(^*)$ are hereafter omitted.

The curl operator is applied two times to equation (9) which is projected in the $\vec{k}$ direction

$$\frac{\mathrm{d}}{\mathrm{d}t}\Delta w = Ra\,Pr\,\Delta_1\theta + Pr\,\Delta^2 w, \tag{10}$$

where

$$\Delta_1 \equiv \frac{\partial}{\partial x} + \frac{\partial}{\partial y}, \quad D \equiv \frac{\partial}{\partial z}$$

w and θ are now developed in normal modes as

$$\theta = T(z)\mathrm{e}^{\mathrm{i}(a_x x + a_y y)}\mathrm{e}^{st} \quad \text{and} \quad w = W(z)\mathrm{e}^{\mathrm{i}(a_x x + a_y y)}\mathrm{e}^{st}.$$

Introducing $a = \sqrt{a_x^2 + a_y^2}$ neutral stability conditions imply:

$$D\Theta W = (D^2 - a^2)T, \tag{11}$$

$$(D^2 - a^2)^2 W = a^2 RaT, \tag{12}$$

where $D\Theta$ is the gradient of the temperature profile corresponding to the nonperturbed state: $D\Theta = (1/2) - z$. We thus have for (11):

$$\left(\frac{1}{2} - z\right)W = (D^2 - a^2)T \tag{13}$$

$T(z)$ is then developed in Fourier series

$$T(z) = \sum_{n=1}^{\infty} A_n \sin(n\pi z) \tag{14}$$

and is introduced into (12) and solved for $W(z)$

$$W(z) = a^2 Ra \sum_{n=1}^{\infty} A_n \left[B_n \cosh(az) + C_n \sinh(az) + D_n z \sinh(az) + E_n z \cosh(az) + \frac{\sin(n\pi z)}{N_n^2} \right] \tag{15}$$

with $N_n = (n\pi)^2 + a^2$.

The coefficients A_n, B_n, C_n, D_n and E_n are determined from the boundary conditions on velocity: $W = DW = 0$ at $z = 0$, $z = 1$, this gives:

$$B_n = 0, \tag{16}$$

$$C_n = \frac{a + (-1)^n \sinh(a)}{\sinh^2(a) - a^2} \frac{n\pi}{N_n^2}, \tag{17}$$

$$D_n = C_n \frac{a\cosh(a) - \sinh(a)}{\sinh(a)} + \frac{n\pi}{N_n^2} \frac{\cosh(a)}{\sinh(a)}, \tag{18}$$

$$E_n = -\left(aC_n + \frac{n\pi}{N_n^2} \right). \tag{19}$$

T and W are then substituted into (13) to yield

$$\sum_{n=1}^{\infty} A_n(-N_n) \sin(n\pi z) = a^2 Ra \sum_{n=1}^{\infty} A_n \left[C_n \left(\frac{1}{2} - z \right) \sinh(az) + D_n z \left(\frac{1}{2} - z \right) \sinh(az) + E_n z \left(\frac{1}{2} - z \right) \cosh(az) + \left(\frac{1}{2} - z \right) \frac{\sin(n\pi z)}{Nn^2} \right]. \tag{20}$$

This expression, as well as the values of A_n, B_n, C_n, D_n and E_n, are different from those obtained by Debler [11], though a similar procedure has been used here.

The equality (20) should be satisfied for $A_n \neq 0$ $\forall n$. For this, we have used the conventional closure for equations containing variables expressed in Fourier series: by multiplying (20) by $\sin(m\pi z)$ and then integrating between 0 and 1

$$\int_0^1 (-N_n) \sin(n\pi z) \sin(m\pi z)\, dz = a^2 Ra \int_0^1 \left[\left(\frac{1}{2} - z \right) \left(C_n \sinh(az) + \frac{\sin(n\pi z)}{Nn^2} \right) + z \left(\frac{1}{2} - z \right) \left(D_n \sinh(az) + E_n \cosh(az) \right) \right] \times \sin(m\pi z)\, dz. \tag{21}$$

(21) must be satisfied $\forall n$, m in order for $A_n \neq 0$. This is equivalent to

$$\det_{m,n} |(21)| = 0. \tag{22}$$

From this equality we deduce a law of the type $Ra = f(a)$, and thus (22) is reduced to a second-order system of equations in m and n. For the classical Rayleigh–Bénard problem the first-order approximation is relatively precise, in the specific case of volume heat generation. Roberts [10] has shown that for the stability analysis of the conductive state one needs to study just the two first steady modes.

$$\mathscr{D} = \begin{vmatrix} \frac{N_1}{2a^2 Ra} + 1/1 & 1/2 \\ 2/1 & \frac{N_2}{2a^2 Ra} + 2/2 \end{vmatrix} \tag{23}$$

with

$$n/m = \int_0^1 \left[\left(\frac{1}{2} - z \right) \left(C_n \sinh(az) + \frac{\sin(n\pi z)}{Nn^2} \right) + z \left(\frac{1}{2} - z \right) (D_n \sinh(az) + E_n \cosh(az)) \right] \times \sin(m\pi z)\, dz. \tag{24}$$

The solution of $\mathscr{D} = 0$ is the curve of marginal stability (Fig. 2), yielding a critical Rayleigh number $Ra_c = 37\,230$ for a critical wave number $a_c = 4$. The value of the critical wave number is similar to those found in linear stability analysis of Rayleigh–Bènard thermoconvective instability; however, the value of the critical Rayleigh number is much higher than in the classical Rayleigh–Bènard configuration, where it is around 1700. This discrepancy is due to the fact that the Rayleigh number here is based on a volume power density, whereas it is usually based on the characteristic temperature difference in the problem. However, comparison can be made with a classical Rayleigh–Bènard configuration [12,13] corresponding to the upper half of the cavity ($d/2$ deep) with upper rigid boundary and

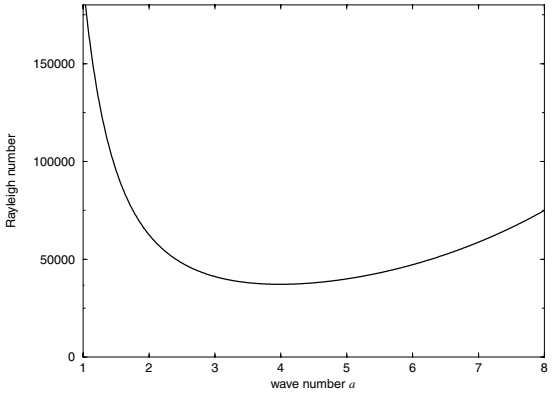

Fig. 2. Marginal stability curve for the uncontrolled system.

lower free boundary where the associated critical Rayleigh number is 1101. In this case the temperature at the upper boundary is the cold temperature and the temperature at the lower boundary is equal to the maximum value of the parabolic temperature profile, $\dot{q}d^2/8\kappa$. The main difference, however, between these two cases is that here we have a semi-parabolic conductive temperature distribution within the fluid layer, whereas a linear temperature profile is usually considered in the classical Rayleigh–Bènard convection. If we write the classical Rayleigh number (i.e., in terms of temperature difference) associated to the critical state of the present configuration:

$$Ra_{\text{classical}} = \frac{\alpha g \Delta T d_1^2}{\nu\kappa},$$

$$\text{with} \quad \Delta T = \frac{\dot{q}_{\text{critical}} d^3}{8\kappa} \quad \text{and} \quad d_1 = \frac{d}{2},$$

$$\dot{q}_{\text{critical}} = \frac{Ra_c \kappa^2 \nu}{\alpha g d^5},$$

which gives rise to a critical value for Rayleigh number as

$$Ra_{\text{classical}} = \frac{Ra_c}{64} = 581.75. \tag{25}$$

The conclusion is that, for the same temperature difference between the boundary planes the parabolic temperature distribution is less stable than the linear one, since the z-component of the temperature gradient is not constant. In the pure Rayleigh–Bénard configuration the temperature gradient is constant and equal to $\dot{q}_{\text{critical}} d/4\kappa$ everywhere in the fluid layer, while in the present configuration the temperature gradient varies from 0 (center of the cavity) to $\dot{q}_{\text{critical}} d/2\kappa$ (on the wall). Therefore the maximun gradient value in the present case is twice larger than that of the pure Rayleigh–Bénard configuration. This explains the ratio $\simeq 0.5$ between the two critical Rayleigh numbers.

3. Linear stability analysis: controlled cavity

By introducing a control loop, we aim to retard the marginal instability, i.e., to push the critical Rayleigh number to higher values. The control strategy used here is based on proportional feedback, a kind of control already used by Tang et al. [6]. The choice of the controlled variable is guided by our goal. We aim at obtaining a conductive temperature distribution in the fluid layer for Ra values above the Ra_c of the uncontrolled system. Therefore, the difference between the real temperature (θ convective) and the temperature in the pure conductive case (θ_{cond}) is tracked (in time) at a given z-position inside the fluid layer. The action variable is the volume heating power dissipated in the fluid. The volume heating thus applied on the fluid layer is conditioned on the value of $\theta - \theta_{\text{cond}}$ at a given z-position z_i. θ_{cond} is known for any z_i, since it is determined by the analytical solution of the conductive problem (2). The optimal position for data measurement is determined from the linear stability analysis.

3.1. Stability limits of the controlled system

The equations governing this system are the same as those for the uncontrolled case (Section 2.2). The control strategy is integrated into the expression of the source term $\dot{q}$, which now has two parts. The first is a constant and identical to $\dot{q}$ in Section 2.2: $\dot{q}_1 = \sigma E^2/\rho C_p$. The second term corresponds to the modulation term of $\dot{q}_1$ determined by the control loop: $\dot{q}_2 = G_d(\theta_{z_i} - \theta_{\text{cond}_{z_i}})$, where z_i designates the z-position where data is extracted and G_d is the proportional gain of control whose dimension is $[s^{-1}]$. The source term in the equation of energy is then expressed as:

$$\dot{q} = \frac{\sigma E^2}{\rho C_p} - G_d(\theta_{z_i} - \theta_{\text{cond}_{z_i}}). \tag{26}$$

Mathematically this expression of the source term can be negative. In this theoretical part of the study the conductive state is perturbed by infinitesimal disturbances so that $\theta_{z_i} - \theta_{\text{cond}_{z_i}} \ll \theta_{\text{cond}_{z_i}}$. The aim of this part is to find the new stability limits of the conductive state when the control module is activated. Therefore for a given value of $\dot{q}$ we will choose the smallest value of G_d for which the configuration remains subcritical. Consequently in the case of infinitesimal perturbances $\dot{q}_2 < \dot{q}_1$ which leads to $\dot{q} > 0$. The mathematical procedure for the stability analysis is similar to that developed in Section 2.2, and the shifting of the stability curve as a function of G_d and z_i is sought. The system of equations to solve is:

$$\begin{aligned}
&\frac{d\theta}{dt} = \vec{\nabla}.(\kappa\vec{\nabla}\theta) + \dot{q}_1 - G_d(\theta_{z_i} - \theta_{\text{cond}_{z_i}}),\\
&\frac{d\vec{v}}{dt} = -\vec{\nabla}\left(\frac{p}{\bar{\rho}} + gz\right) - \alpha g\theta\vec{k} + \frac{\vec{\nabla}.\bar{\bar{\tau}}}{\bar{\rho}},\\
&\vec{\nabla}.(\rho\vec{v}) = 0.
\end{aligned} \tag{27}$$

They are perturbed by infinitesimal perturbations and after linearization become:

$$\begin{aligned}
&\frac{\partial\theta'}{\partial t} + w'\frac{\partial\Theta}{\partial z} = \kappa\Delta\theta' - G_d\theta'_{z_i},\\
&\frac{d\vec{v}'}{dt} = -\vec{\nabla}\left(\frac{p'}{\bar{\rho}}\right) - \alpha g\theta'\vec{k} + \nu\Delta\vec{v}'.
\end{aligned} \tag{28}$$

They are then nondimensionalized by the same variables as for the uncontrolled cavity to yield:

$$\frac{\partial\theta'^*}{\partial t^*} + w'^* \frac{\partial \Theta^*}{\partial z^*} = \Delta^*\theta'^* - G\theta'^*_{z_i},$$
$$\frac{\mathrm{d}\vec{v}'^*}{\mathrm{d}t^*} = -\nabla^* p'^* - Ra\,Pr\,\theta'^*\vec{k} + Pr\Delta^*\vec{v}'^*. \tag{29}$$

Since $\Delta_1\Theta_{zi} = \Delta_1\Theta = 0$, the system of equations to solve reduces to:

$$D\Theta W = (D^2 - a^2)T - GT(z_i),$$
$$(D^2 - a^2)^2 W = a^2 Ra\,T. \tag{30}$$

The second equation of (30) is similar to (12). By developing $T(z)$ in Fourier series one gets the same expression for $W(z)$ as in the uncontrolled system, as well as for the value of the coefficients B_n, C_n, D_n and E_n. By introducing $T(z)$ and $W(z)$ in the first equation of system (30), the dispersion relation $Ra = f(a)$ is obtained in which the value of G and the position z_i at which the data are extracted appear as control parameters

$$\sum_{n=1}^{\infty} A_n(-N_n)\sin(n\pi z)$$
$$= a^2 Ra \sum_{n=1}^{\infty} A_n \left[C_n\left(\frac{1}{2} - z\right)\sinh(az) + D_n z\left(\frac{1}{2} - z\right)\sinh(az) + E_n z\left(\frac{1}{2} - z\right)\cosh(az) + \left(\frac{1}{2} - z\right)\frac{\sin(n\pi z)}{Nn^2}\right] - G\sum_{n=1}^{\infty} A_n \sin(n\pi z_i). \tag{31}$$

In order to obtain nontrivial solutions for any $An \neq 0$ $\forall n$, it is required that

$$\int_0^1 (-N_n)\sin(n\pi z)\sin(m\pi z)\,\mathrm{d}z$$
$$= a^2 Ra \int_0^1 \left[\left(\frac{1}{2} - z\right)\left(C_n \sinh(az) + \frac{\sin(n\pi z)}{Nn^2}\right) + z\left(\frac{1}{2} - z\right)\left(D_n \sinh(az) + E_n \cosh(az)\right)\sin(m\pi z)\right]\mathrm{d}z. + \int_0^1 G\sin(n\pi z i)\sin(m\pi z)\,\mathrm{d}z. \tag{32}$$

This is equivalent to

$$\mathscr{D} = \begin{vmatrix} \frac{1}{a^2 Ra}\left(\frac{N_1}{2} + \frac{2\sin(\pi z_i)G}{\pi}\right) + 1/1 & 1/2 \\ 2/1 + \frac{2G\sin(2\pi z_i)}{\pi a^2 Ra} & \frac{N_2}{2a^2 Ra} + 2/2 \end{vmatrix}. \tag{33}$$

The value of m/n is the same as in the uncontrolled system (24).

The uncontrolled system will be recovered for $G = 0$. Computations have been carried out for four values of z_i and different values of G. Figs. 3 and 4 show marginal stability curves for $z_i = 3/4$ and $1/2$ and

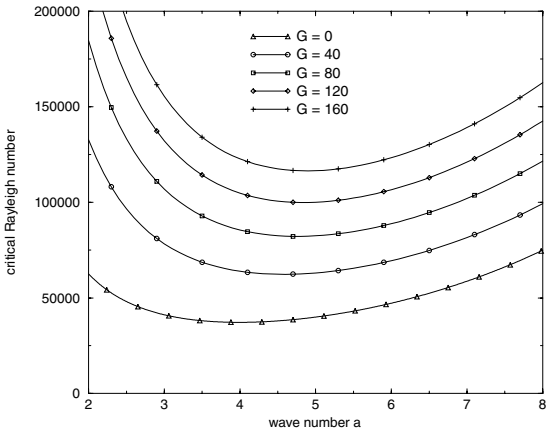

Fig. 3. Marginal stability curve with control at $z_i = 3/4$ and for different dimensionless feedback gains G.

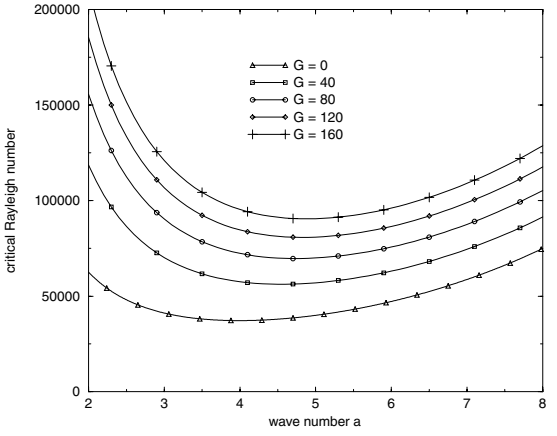

Fig. 4. Marginal stability curve with control at $z_i = 1/2$ and for different dimensionless feedback gains G.

different values of G. Notice that whatever the positive gain value and the z-position of the temperature probe, the introduction of the control loop stabilizes the system. No matter which z_i is chosen, the larger the gain, the higher the value of critical Rayleigh number. It can also be noticed that as the threshold of instability increases, the critical wave number a_c moves towards higher values. For constant G it is more effective to base the control on the data location $z_i = 3/4$ than on another z-position, as can be seen in Fig. 5. This can be intuitively linked to the fact that the center of the cellular structures of the convective movement is located at $z = 3/4$, which is the midline of the upper half of the cavity. In the above computation it is assumed that the principle of the exchange of stability is valid (time-independent perturbations). At high Rayleigh numbers this hypothesis can be violated, and therefore the stability of the system under time-dependent perturbations

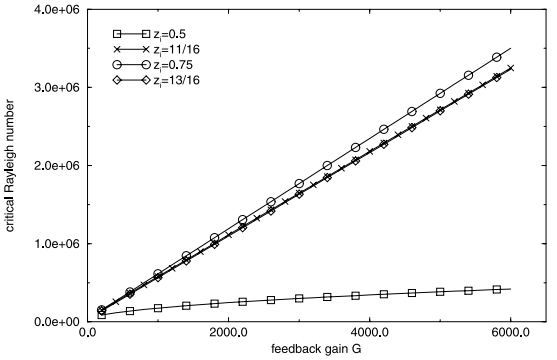

Fig. 5. Evolution of Ra_c as a function of dimensionless feedback gain G for four z_i values.

must be studied in order to define the domain of validity of the curves of Fig. 5.

4. Numerical simulations

4.1. General conditions

The Navier–Stokes, continuity and energy equations were solved using the dimensional finite volume numerical code ESTET [14]. The numerical scheme used is SIMPLEC and convective terms are estimated by a QUICK-UPWIND scheme. The theoretical analysis in Section 3 was applied to a laterally unbounded fluid layer. However, the code used here requires finite lateral boundary conditions. In order to approach the theoretical case, a large-aspect-ratio (10:1) thin fluid layer was considered in the computations (Fig. 1(b)). In future experimentations and three-dimensional simulations the $\vec{j}$-direction will be dedicated to the shorter horizontal direction which will be the direction of orientation of the structures that will appear. Thus, we restrict attention to a two-dimensional fluid layer in the $(\vec{i},\vec{k})$ plane with symmetry conditions imposed in the $\vec{j}$ direction. This type of condition implies conservation of vorticity in $\vec{j}$ direction. The grid size in the $(\vec{i},\vec{k})$ cross-section is 151×63. It is refined on the vicinity of the upper, lower and lateral walls and the mesh size is increased progressively by a ratio of $4/3$ towards the center of the cavity. The working fluid is water ($Pr = 7.48$).

The temperature and velocity boundary conditions are:

$$\begin{cases} \theta = 0, & z = 0, 1 \\ \frac{\partial\theta}{\partial x} = 0, & x = -5, 5, \end{cases} \qquad \begin{cases} \vec{v} = \vec{0}, & z = 0, 1, \\ \vec{v} = \vec{0}, & z = -5, 5. \end{cases} \tag{34}$$

All the results will be shown in dimensionless form (as in Section 2) and (*) will be omitted.

4.2. Validation of the numerical code

The validity of the code is verified by searching the value of the critical Rayleigh number of the first bifurcation from the conductive state to the convective state. The heating power is adjusted so that the Rayleigh number is around its critical value. We want to verify that below this value the fluid remains motionless and above it thermoconvective motion sets in.

4.2.1. Subcritical state

The heating power is adjusted so that the associated Rayleigh number becomes subcritical. The Rayleigh number for the specific case presented here is $Ra = 37\,000$ and the evolution of the vertical component of the velocity at $z = 0.718$ is shown in Fig. 6. The velocity perturbations oscillate around zero mean velocity and are damped at longer time intervals. The amplitude of oscillations remains infinitesimal, at the limit of the precision of the numerical code or the machine. This is confirmed by the time evolution of the instantaneous temperature at $z = 0.718$ during the transitory phase as shown in Fig. 7: the transitory phase evolves exponentially, as is a characteristic of a conductive regime. It is to notice that the temperature converges 10 times more rapidly then the vertical component of the velocity. Fig. 8 plots the nondimensional value of the vertical velocity component as a function of x for $z = 3/4$ at the last time step calculated (i.e., when the thermal steady-state is reached). This value is zero everywhere except in the vicinity of the lateral walls and even in this region it is on the order of 6×10^{-3}, this solution is time invariant there is no propagation of the lateral perturbation in the heart of the cavity. Finally, the comparison of the

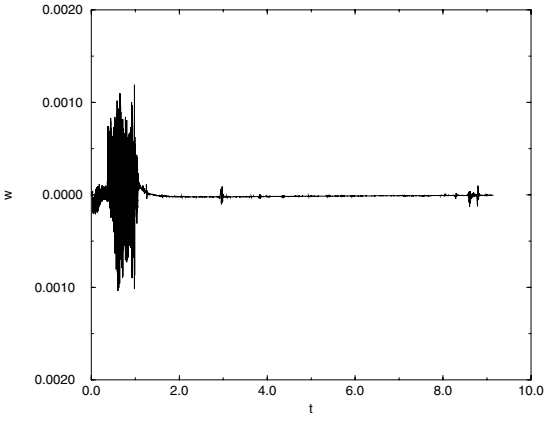

Fig. 6. Time evolution of the vertical component of velocity at $z = 0.718$, $x = 0$, $Ra = 37\,000$.

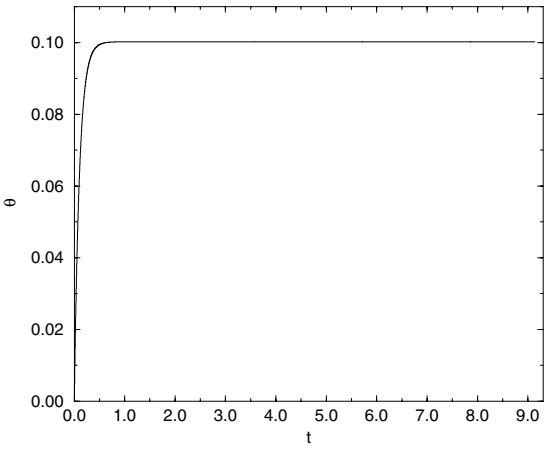

Fig. 7. Time evolution of temperature at $z = 0.718$, $x = 0$, $Ra = 37000$.

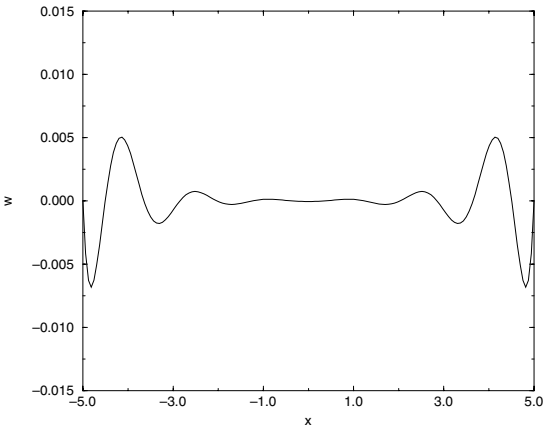

Fig. 8. Distribution of the vertical component of velocity as a function of x at $z = 3/4$, $t = 9.1$, $Ra = 37000$.

computed temperature profile and the theoretical parabolic conductive profile (in Fig. 9) at the last time step shows that the system is definitively in a conductive state.

4.2.2. Weakly supercritical state

Fig. 10 represents the time evolution of the vertical velocity component for $Ra = 40000$ at $z = 0.718$, $x = 0$. Notice that the velocity has stabilized at a nonzero value, which implies that the flow solution is steady and that the stability threshold has been reached. This conclusion is confirmed by the temperature profile as a function of z (Fig. 11) and the velocity profile as a function of x (Fig. 12) at the last time step simulated (i.e., when both thermal and dynamic steady-states are reached). The temperature profile nevertheless remains similar to the conductive temperature profile. This can

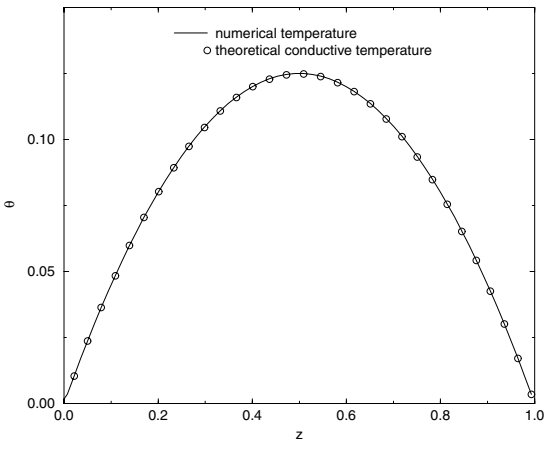

Fig. 9. Temperature profile across the cavity at $x = 0$, $t = 9.1$, $Ra = 37000$.

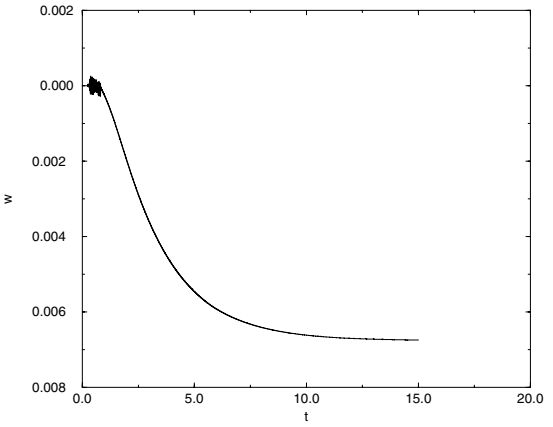

Fig. 10. Time evolution of the vertical component of velocity at $z = 0.718$, $x = 0$, $Ra = 40000$.

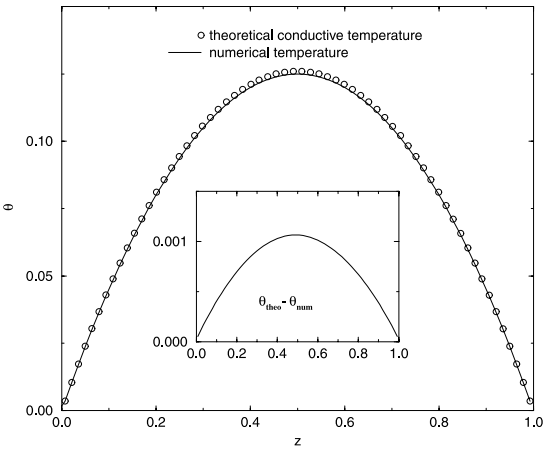

Fig. 11. Temperature profile across the cavity at $x = 0$, $t = 15$, $Ra = 40000$.

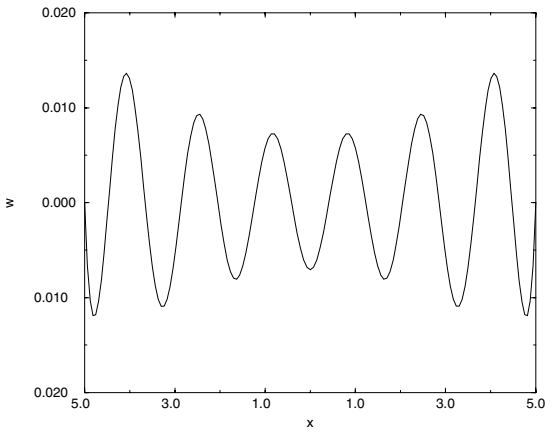

Fig. 12. Distribution of the vertical component of the velocity as a function of x for $z = 3/4$, $t = 15$, $Ra = 40\,000$.

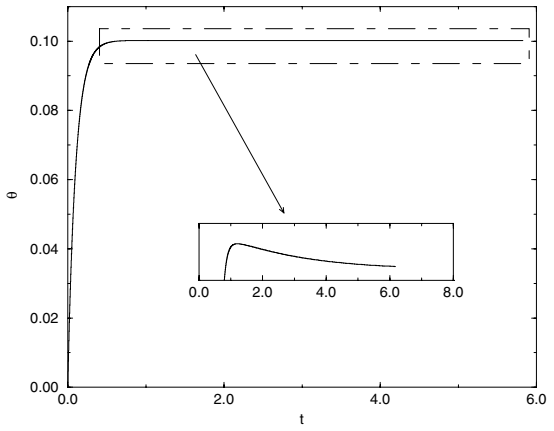

Fig. 13. Time evolution of the temperature at $z = 0.718$, $x = 0$, $Ra = 40\,000$.

be readily explained from energy considerations: at the beginning the system dissipates by conduction the energy received (see Fig. 13 for the temporal evolution of the temperature), but when the conduction process can no longer dissipate this energy completely, the extra thermal energy is converted into mechanical energy, in the present case at $t \simeq 1$. At this point, the Rayleigh number is close to its critical value and the thermal energy converted to mechanical energy is weak, so that the temperature profile deviates only slightly from that of conductive state. Fig. 14 plots, for the cavity, the isovorticity lines (left) and the isocontour lines (right) of the difference between the computed temperature field and the theoretical conductive temperature at $Ra = 40\,000$. This appears as a weak but cellularly organized and time-independent movement. The temperature isocontour lines plotted on the right-hand side of the figure show that the temperature profile is modified throughout the cavity but at different rates. In the bottom half, the isocontour lines remain parallel showing that the energy state has changed but energy is still being dissipated by conduction. In the upper half of the cavity, the waviness of the isocontour lines shows the thermal signature of the convective structures. From the above verification, it can be concluded that the numerical code is precise enough to allow prediction of the flow structure and evaluation of the control strategy.

4.3. Numerical simulation of the control loop

In this section, we discuss the implementation of the control strategy developed in Section 3 in the numerical procedure. The operational mode chosen is to start the computation without control and let the flow regime be established. Then the solution $[\theta(x,y,z,t_0),\ \vec{v}(x,y,z,t_0),\ P(x,y,z,t_0)]$ obtained is chosen as the initial conditions for the computations with control strategy. The control loop may first bring the system near the reference state and then, will counter the convective starts and therefore make the system oscillate around the conductive state. The amplitude of oscillations is connected to the accuracy of the loop. For each time step we define the new power that must be injected in the system for each fluid column, i.e., within each mesh column. The numerical code has already proven able to handle time- and space-dependent boundary conditions defined by data extracted from the previous time step [15]. The feedback loop is

$$\dot{q}_2(x,y,z,t+1) = G\left(\theta\left(x,y,\frac{3}{4},t\right) - \theta_{\mathrm{cond}}\left(x,y,\frac{3}{4},t\right)\right). \tag{35}$$

Here, before the activation of the control loop the difference between the convective state and its associated conductive state is no more infinitesimal. It is evident that the system cannot be cooled in its volume, we can only stop heating. To avoid this a filter is fixed downstream of the control loop:

Fig. 14. Isocontour lines of vorticity (left) and isocontour lines of difference between the calculated temperature profile and theoretical conductive one (right), $t = 15$, $Ra = 40\,000$.

$$\begin{cases} \text{If } \dot{q}_2 < \dot{q}_1, & \text{then } \dot{q} = \dot{q}_1 - \dot{q}_2, \\ \text{If } \dot{q}_2 > \dot{q}_1, & \text{then } \dot{q} = 0. \end{cases} \quad (36)$$

The filter history shows that the filter is only necessary for the three first steps of action. This definition of the loop shows that its efficiency will be highly connected to the precision of temperature measurements: the more precisely we know the temperature in the fluid, the smaller is the difference between controlled state and the theoretical conductive state. In the numerical simulations carried out for confirmation of the efficiency of the loop, the measurement error is not taken into account. The loop was tested on two different configurations. In the first the strategy was applied to the convective case to check the value of Ra_c ($Ra = 40\,000$). The peculiarity of this case is its steadiness. Then the strategy was tested on a case beyond the threshold of a new bifurcation, when as a result natural convection characterized by a time-dependent velocity field is established.

4.3.1. Computations for small Rayleigh number

The Rayleigh number for this case is $Ra = 40\,000$ and the corresponding regime, as shown before, is convective in an uncontrolled configuration. However, as can be seen in Fig. 3, the regime is situated in the stable zone if a feedback gain of $G = 30$ is applied. We start to apply the control at $t_0 = 15$. Fig. 15 shows that a significant decrease in the vertical component of the velocity at $z = 0.718$ is achieved 0.2 time units after the control is applied. A closer look at the axial profile of the vertical velocity (Fig. 16) shows that some vertical movements of the fluid particles still exist in the lateral sides of the cavity; this is attributed to wall effects. The corresponding temperature profile across the cavity span (Fig. 17), collapses on the conductive profile, as is the aim of the control strategy; the purpose was to re-stabilize a conductive temperature profile.

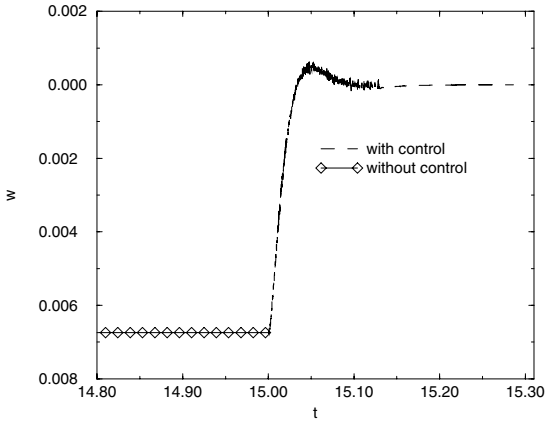

Fig. 15. Time evolution of the vertical velocity component at $z = 0.718$, $x = 0$, $Ra = 40\,000$. Control strategy is applied at $t = 15$ ($G = 30$).

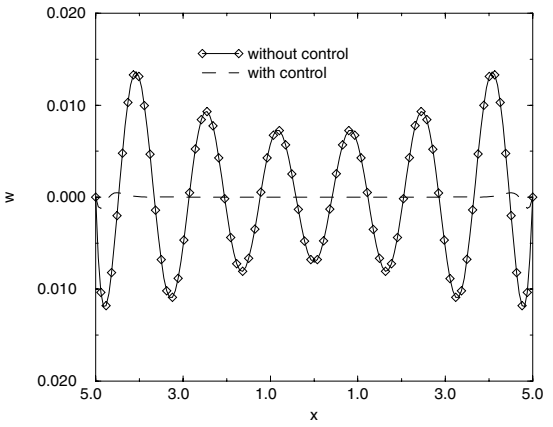

Fig. 16. Distribution of the vertical component of the velocity as a function of x for controlled and uncontrolled systems, $z = 3/4$, $Ra = 40\,000$, $G = 30$.

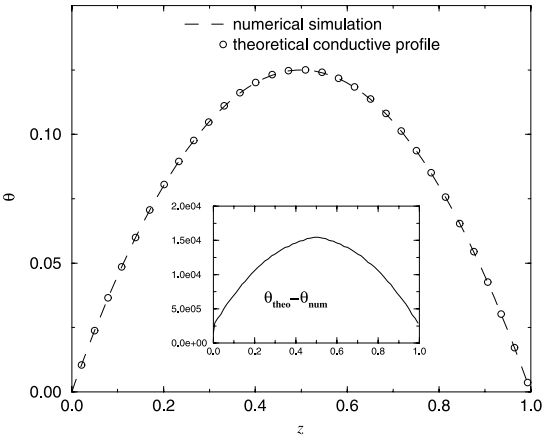

Fig. 17. Temperature across the cavity at $x = 0$ for controlled system, $Ra = 40\,000$, $G = 30$.

4.3.2. Computations for a high Rayleigh number

Computations are repeated for $Ra = 2.4 \times 10^5$. In this case the gain of the control loop is $G = 370$ (Fig. 5). The control strategy is set on at $t_0 = 7.41$. At this time step the convective state is fully established. Fig. 18(a) shows the isocontour lines of velocity (left) and temperature (right). Convective cells are generated in the upper half of the cavity by thermoconvective instability and the vorticity is diffused to some extent into the lower half of the cavity. The isocontour lines of the temperature also show a cellular structure. Fig. 18(b) shows the same domain once the control is applied. On the left side of the figure the fluid domain is motionless: the convective cells have disappeared. On the right the isocontour lines of temperature are parallel horizontal lines, indicating a pure conductive state. These results show

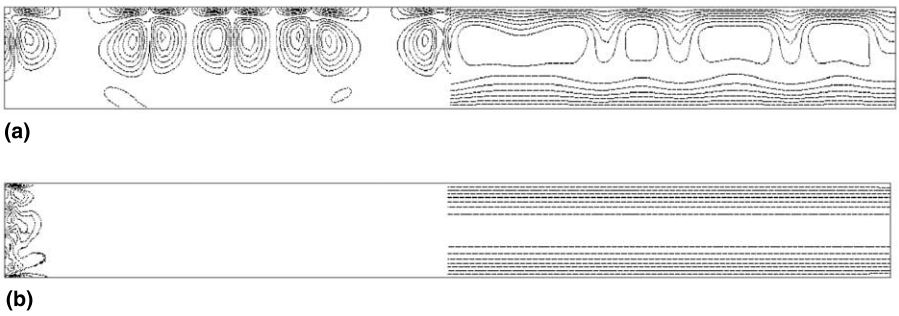

Fig. 18. Isocontour lines of vorticity (left) and temperature (right): (a) uncontrolled case ($t = 7.4$); (b) controlled case ($G = 370$, $t = 7.6$), $Ra = 2.4 \times 10^5$.

clearly that through the active control, the instability threshold has been pushed up in such a way that the state of the system becomes subcritical and hence a conductive state is re-established.

Re-stabilization of the system is also apparent in Fig. 19, where the transverse profile of the temperature is plotted at $x = 0.18$ for the controlled and uncontrolled cases. In the uncontrolled case the maximum value of temperature has moved towards the upper wall as a result of mixing due to the convective cells superposed on the conductive mode of heat transfer. The axial (x) distribution of the transverse component of velocity w is shown in Fig. 20 for both the controlled and uncontrolled cases. In the latter case the nondimensional velocity varies between $+20$ and -55, whereas once the control strategy is applied the transverse velocity is completely suppressed. This shows that the system has been re-stabilized and pure conductive heat transfer restored. The temporal evolution of the transverse velocity monitored at observation position $z = 0.718$ (Fig. 21)

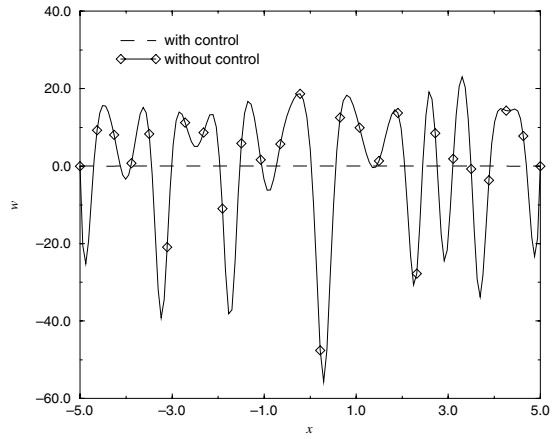

Fig. 20. Distribution of the vertical component of the velocity as a function of x for $z = 3/4$ for controlled ($G = 370$) and uncontrolled cases, $Ra = 2.4 \times 10^5$.

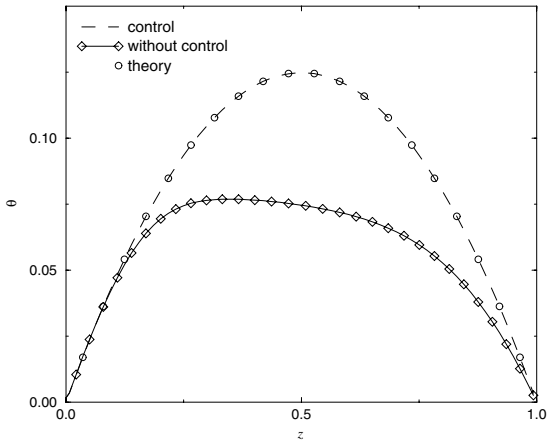

Fig. 19. Temperature distribution across the cavity at $x = 0$ for controlled ($G = 370$) and uncontrolled cases, $Ra = 2.4 \times 10^5$.

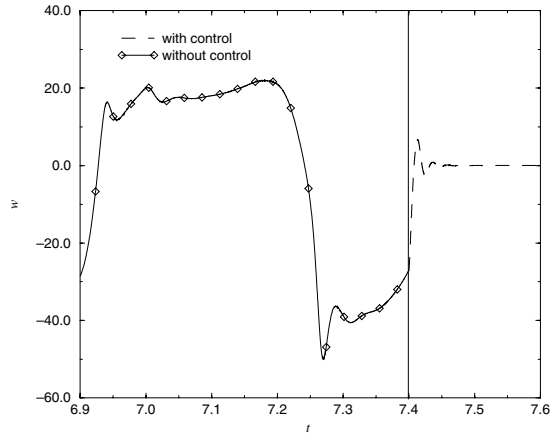

Fig. 21. Time evolution of the vertical velocity component at $x = 0.18$, $z = 0.718$. Control strategy is applied at $t = 7.4$, $Ra = 2.4 \times 10^5$, $G = 370$.

also indicates the complete success of the control procedure. The velocity varies with time until $t_0 = 7.41$, when the feedback control is applied to the system. After a short response time (less than 10% of time constant of the system), the velocity component is completely suppressed and remains so thereafter.

In summary, for the high Rayleigh number case the feedback control has been shown to be effective in suppressing the convective cells, returning the fluid to a motionless state and restoring the temperature profile to the conductive mode. These observations are similar to the low Rayleigh number case. However, the effects are more spectacular in the high Rayleigh number case since the velocities are 1000 times greater and the temperature deviation from conductive state is 100 times larger than in the low Rayleigh number case.

In Fig. 18(b) some vorticity zones persist even after the application of the feedback control. This is due to boundary effects, whose vorticity values are much less than the mean vorticity (1%) in the uncontrolled conditions.

5. Conclusions

Through a linear stability analysis we have established the critical Rayleigh number for a fluid layer between two isothermal planes and subjected to an internal dissipation of heat. We have chosen a control strategy aimed at delaying the appearance of natural convection and have proven its theoretical efficiency through an stability analysis.

A numerical study has given us the opportunity to corroborate the results theoretically established concerning the uncontrolled value of the critical Rayleigh number. Our numerical simulation of the control loop has proven to be completely satisfactory.

Acknowledgements

The authors highly acknowledge the support of the Ministery of Research and Higher Education for this work in the framework of AMETH program.

References

[1] R.D. Joslin, R.A. Nicolaides, M.Y. Hussaini, M.D. Gunzburger, Active control of boundary-layer instabilities: use of sensors and spectral controller, AIAA J. 33 (8) (1995) 1521–1523.

[2] R.D. Joslin, R.A. Nicolaides, M.Y. Hussaini, M.D. Gunzburger, A methodology for the automated optimal control of flows including transitional flows, in: 1996 ASME Fluids Engineering Division Conference, San Diego, California, 7–11 July, 1996, pp. 287–294.

[3] H. Choi, P. Moin, J. Kim, Active turbulence control for drag reduction in wall bounded flows, J. Fluid Mech. 262 (1994) 75–110.

[4] L.D. Kral, H.F. Fasel, Numerical investigation of three-dimensional active control of boundary transition, AIAA J. 29-9 (1991) 1407–1417.

[5] J. Singer, H.H. Bau, Active control of convection, Phys. Fluids A 3 (1991) 2859–2865.

[6] J. Tang, H.H. Bau, Stabilization of the no-motion state of a horizontal fluid layer heated from below with Joule heating, J. Heat Transfer, Trans. ASME 117 (1995) 329–333.

[7] L.E. Howle, Control of Rayleigh–Bénard convection in a small-aspect-ratio container, Int. J. Heat Mass Transfer 40-4 (1997) 817–822.

[8] J. El-Hajal, Etude expérimentale et numérique de la convection mixte dans un écoulement de Poiseuille en présence d'une dissipation volumique d'énergie par conduction électrique directe, Doctoral dissertation, University of Nantes, France, 1997.

[9] A. Ould El moctar, H. Peerhossaini, J.P. Bardon, Numerical and experimental investigation of direct electric conduction in a channel flow, Int. J. Heat Mass Transfer 39-5 (1996) 975–993.

[10] P.H. Roberts, Convection in horizontal layers with internal heat generation: theory, J. Fluid Mech. 30 (1967) 33–49.

[11] W.R. Debler, On the analogy between thermal and rotational hydrodynamic stability, J. Fluid Mech. 24 (1966) 165–176.

[12] S. Chandrasekhar, Hydrodynamic and Hydromagnetic Stability, Dover, New York, 1981.

[13] P.G. Drazin, W.H. Reid, Hydrodynamic Stability, Cambridge University Press, Cambridge, 1995.

[14] J.D. Mattei, Estet. manuel de l'utilisateur, EDF-DER (1995).

[15] T. Marimbordes, A. Ould El moctar, H. Peerhossaini, Perturbation d'un écoulement de Poiseuille isotherme par un apport pariétal d'énergie: simulations numériques, in: Séminaire AMETH, 25 Novembre 1998, Societé française de Thermique, Paris, 1998.